THE ISOTHERMAL OUTFLOW IN THE HIGH-MASS STAR-FORMING REGION G240.31+0.07

Junhao Liu[1] and Keping Qiu[1]

[1]School of Astronomy & Space Science, Nanjing University, Nanjing, P.R.China

ABSTRACT

We present Atacama Pathfinder Experiment (APEX) observations toward the massive star-forming region G240.31+0.07 in the CO (3-2), (6-5), and (7-6) lines. These lines have traced the previously detected bipolar outflow and show similarity in morphology. The line ratios of the four transitions are remarkably constant with the outflow velocity. Using the CO (3-2), (6-5), and (7-6) data and the complementary CO (2-1) data, we estimate the physical parameters of the G240.31+0.07 outflow as a function of gas velocity, by the means of the rotalation diagram analysis and the large velocity gradient (LVG) analysis. Our results reveal that the temperature of the outflow has an almost constant value of ~ 50 K, warmer than previously adopted temperatures of ~ 30 K. The isothermal state is consistent with the wide-angle wind-driven model. We also find a decreasing trend of CO column density with gas velocity. In addition, the modeling results reveal that the outflowing gas is thermalized and no upper limits to the gas density could be derived. The lower limits of gas density are $n_{\rm low} \sim 10^5$ cm^{-3}. A decreasing gas density with velocity is detected if assumptions of a constant CO abundance ratio and a constant velocity gradient are valid.

Keywords: ISM: individual objects(G240.31+0.07) - ISM: jets and outflows - stars: formation

Corresponding author: Keping Qiu
kpqiu@nju.edu.cn

1. INTRODUCTION

Bipolar molecular outflows, mostly observed via CO, HCO^+ and their isotopes, are a common phenomenon associated with young stellar objects (YSOs) of all masses (Zhang et al. 2001; Beuther et al. 2002a; Wu et al. 2004, 2005; Maud et al. 2015). It is believed that molecular outflows trace the accretion-powered ejections in sites of low-mass star formation. As molecular outflows impact the surrounding material and the parent cloud significantly, they play an important role in the star formation process. Though molecular outflows have been well studied, the driving mechanism of molecular outflows remains unknown. Molecular outflows from low-mass protostars were thought to be entrained by wide-angle winds (Shu et al. 1991; Lee et al. 2001), or by jet bow shocks (Raga & Cabrit 1993; Masson & Chernin 1993; Lee et al. 2001). Though the wind-driven model and the jet-driven model can each explain the characteristics of some observed outflows, none of them are capable of producing the observed features of all types of outflows (Lee et al. 2000, 2002). In order to explain different features of various types of outflows associated with low-mass YSOs simultaneously, two-component models with both highly collimated jet and wide-angle wind have been developed (Shu et al. 2000; Banerjee & Pudritz 2006; Pudritz et al. 2006; Shang et al. 2006; Pudritz et al. 2007; Machida et al. 2008).

Massive molecular outflows are more problematic than their low-mass counterparts. Though observations have shown that the morphology and kinematics of some outflows driven by massive YSOs are very similar to the outflows driven by low mass YSOs (Shepherd et al. 1998; Beuther et al. 2002b; Qiu et al. 2009; Ren et al. 2011), there is a lack of detection of extremely collimated outflows and circumstellar disks towards sources more massive than early B-type YSOs (Arce et al. 2007). Thus, it is not clear whether massive stars form as a scaled-up version of low-mass stars or they form in a different way. Due to the rarity and typically large distances of high-mass YSOs, the sample of individual studies towards outflows driven by massive YSOs is still small. And there is little theoretical work on modeling outflows from high-mass YSOs. Many questions, e.g., how the outflows from massive YSOs are accelerated, how they differ from low-mass outflows, and how they affect the high-mass star-forming processes, are still unanswered. It is essential to address these questions by studying more outflows associated with high-mass star-forming regions.

Most previous studies of outflows have used low-J rotational transitions of CO (transitions up to $J_u = 3$, with upper-state energies E_u up to 30 K), which are easily excited at low temperatures, to characterize the relatively cold and extended molecular gas in morphology and kinematics. These low-J CO emission lines can be easily observed from the ground-based facilities. Due to atmospheric limits, mid-J CO lines (referring to CO (6-5) and CO (7-6) throughout this paper, with E_u up to 150 K), which are less affected by ambient gas, are not commonly observed. In several studies, mid-J CO transitions have been reported to trace the warm gas (T > 50 K) in outflows of low-mass and intermediate-mass YSOs (van Kempen et al. 2009a,b; Yıldız et al. 2012; van Kempen et al. 2016). By comparing multi-line CO observations (both low-J and mid-J) with the results of non-LTE radiative transfer models, the physical properties (temperature, density) of the outflowing gas could be well constrained (Lefloch et al. 2015).

This paper is a follow-up study of the G240.31+0.07 (hereafter G240) outflow (Qiu et al. 2009). We report the 12-m submillimeter Atacama Pathfinder Experiment Telescope[1] (APEX) observations of G240, an active high-mass star-forming region which is associated with the YSO IRAS 07427-2400 and located at a distance of 5.41 kpc (Sakai et al. 2015). It harbors an ultracompact HII region and is associated with OH and H_2O masers (Hughes & MacLeod 1993; Caswell 1997; MacLeod et al. 1998; Migenes et al. 1999; Caswell 2003). Its far-infrared luminosity of $10^{4.7}$ $L_\odot$ is consistent with a spectral type O8.5 zero-age main-sequence star (MacLeod et al. 1998). Qiu et al. (2009) presented a high resolution interferometric study at 1.3 mm and resolved the central part of G240 into three dusty cores MM1, MM2, and MM3. Kumar et al. (2003) mapped the CO (3-2) emission with a 20″ beam and found a prominent bipolar outflow at a position angle (PA) of 132° and a weaker component at PA ∼ 101°. Recently, Qiu et al. (2009) presented a detailed single dish and interferometric study of ^{12}CO (2-1) and ^{13}CO (2-1) emissions and detected a bipolar, wide-angle, quasi-parabolic molecular outflow. In addition, Qiu et al. (2014) reported the detection of an hourglass magnetic field aligned within 20° of the outflow axis.

In this paper, we present a CO multi-transition (2-1, 3-2, 6-5, 7-6) study towards the G240 outflow. With rotation diagram (RD) analysis and large velocity gradient (LVG) calculations, we estimate the physical parameters of the outflow as functions of gas velocity. We then discuss the results of the analyses.

---

[1] The Atacama Pathfinder Experiment Telescope is a collaboration between the Max-Planck-Institut für Radioastronomie, the European Southern Observatory, and the Onsala Space Observatory.

Table 1. Line informations

Line	Frequency	Beam size	σ_{cal} [a]	σ_{rms} [b]	η_s [c]
	GHz	$''$	%	K	
CO (2-1)	230.5380	3.93×3.10 [d]	10	0.08	–
CO (3-2)	345.7960	19.16	15	0.04	0.65
CO (6-5)	691.4731	9.49	20	0.20	0.41
CO (7-6)	806.6518	8.12	30	0.50	0.40

[a] Calibration error.

[b] Average rms in 2 km s^{-1} channels.

[c] Beam efficiency.

[d] Major axis × minor axis.

2. OBSERVATIONS

The observations were performed with the 12 m APEX telescope. The CO (3-2) tansition was observed in 200? using the ? receiver, whereas the CO (6-5) and CO (7-6) lines were observed simultaneously in 2009 with the CHAMP+ receiver. Pointings were checked by comparing these lines with the CO (2-1) data adopted from Qiu et al. (2009), and were found to be within $\sim 7''$ for CO (3-2) and within $\sim 4''$ for CO (6-5) and (7-6). The system temperatures were found to be ? at ? GHz. The ? spectrometer was used as the backend with a resolution of ? kHz (? km s^{-1}). The data were smoothed to 2 km s^{-1}, then the rms noises are of the order 0.03-0.05 K at 345 GHz, 0.15-0.25 K at 691 GHz and 0.40 - 0.60 K at 809 GHz. Beam efficiencies, determined by observations of planets, were 0.65, 0.41 and 0.40 at 345 GHz, 691 GHz and 809 GHz, respectively. The APEX beam sizes are $\sim 19''$ at 345 GHz, $\sim 9''$ at 691 GHz and $\sim 8''$ at 809 GHz. Calibration uncertainties were assumed to be 15 %, 20% and 30% at 345 GHz, 691 GHz and 809 GHz, relatively. These data were complemented with the perviously observed combined data from the Submillimeter Array[2] (SMA) and the Caltech Submillimeter Observatory[3] (CSO) 10.4 m telescope in CO (2-1) (Qiu et al. 2009). The CO (2-1) data has a calibration uncertainty of 10 %, with the rms estimated

to be 0.06-0.10 K in 2 km s^{-1} channels. Table 1 shows a summary of the line informations.

3. RESULTS

3.1. *CO EMISSION MAPS*

The cloud velocity (v_{cloud}) with respect to the local standard of rest is ~ 67.5 km s^{-1} (Kumar et al. 2003). The CO (3-2), (6-5) and (7-6) emissions are detected in velocity ranges from 42 km s^{-1} to 94 km s^{-1}, 44 km s^{-1} to 90 km s^{-1}, and 48 km s^{-1} to 86 km s^{-1}, respectively. Figure 1 shows the integrated low-velocity (LV) and high-velocity (HV) emissions of the four transitions. The same velocity ranges with those in Qiu et al. (2009) were chosen to highlight the LV and HV components of the outflowing gas, except for CO (7-6), which we use a smaller velocity range to show the HV emission because of the relatively low signal-to-noise ratio. The outflow morphologies seen in CO (3-2), (6-5) and (7-6) are very similar: a prominent bipolar outflow at (PA) $\sim 131°$ along with a weaker component at PA $\sim 101°$ is detected. The weaker outflow component is only detected at low velocities, while the prominent component is detected at both low and high velocities. Overall, the CO (3-2), (6-5), (7-6) maps presented in Figure 1 are very similar to the CO (3-2) map presented by Kumar et al. (2003). Due to the limit of angular resolution, the wide-angle structure highlighted by the CO (2-1) emission is not seen in the CO (3-2), (6-5), (7-6) maps.

3.2. *PHYSICAL CONDITIONS OF THE OUTFLOW*

The physical conditions of the outflow could be constrained by comparing the observed line intensities with results of statistical-equilibrium calculations. To study the four lines at the same spatial resolution, we convolved the CO (2-1), (6-5) and (7-6) maps to the same beam size of the CO (3-2) map. The average rms noises are 0.004 K, 0.04 K and 0.10 K for the convolved CO (2-1), (6-5) and (7-6) data, respectively. We then calculated the CO fluxes at (R.A., decl.)$_{J2000}$ = $(07^h44^m52^s.4, -24^d7^m53^s.8)$ and (R.A., decl.)$_{J2000}$ = $(07^h44^m51^s.3, -24^d7^m34^s.6)$ (marked as two crosses in each panel of Figure 1). The two positions are roughly the peak of the high velocity components of each lobe of the convolved maps of the four transitions. We note that the offsets of the peak positions are within $\sim 3''$ for different lines at different velocities. To avoid contaminations from the ambient gas, we limited our analyses to velocity ranges of ≤ 60 km s^{-1} and ≥ 74 km s^{-1}. And we only focused our analyses on the data with high signal-to-noise ratios in velocities ranges of ≥ 48 km s^{-1} and ≤ 86 km s^{-1}. Figure 2 shows the observed line wing ratios of main-beam temperatures (T_{mb}) of different CO
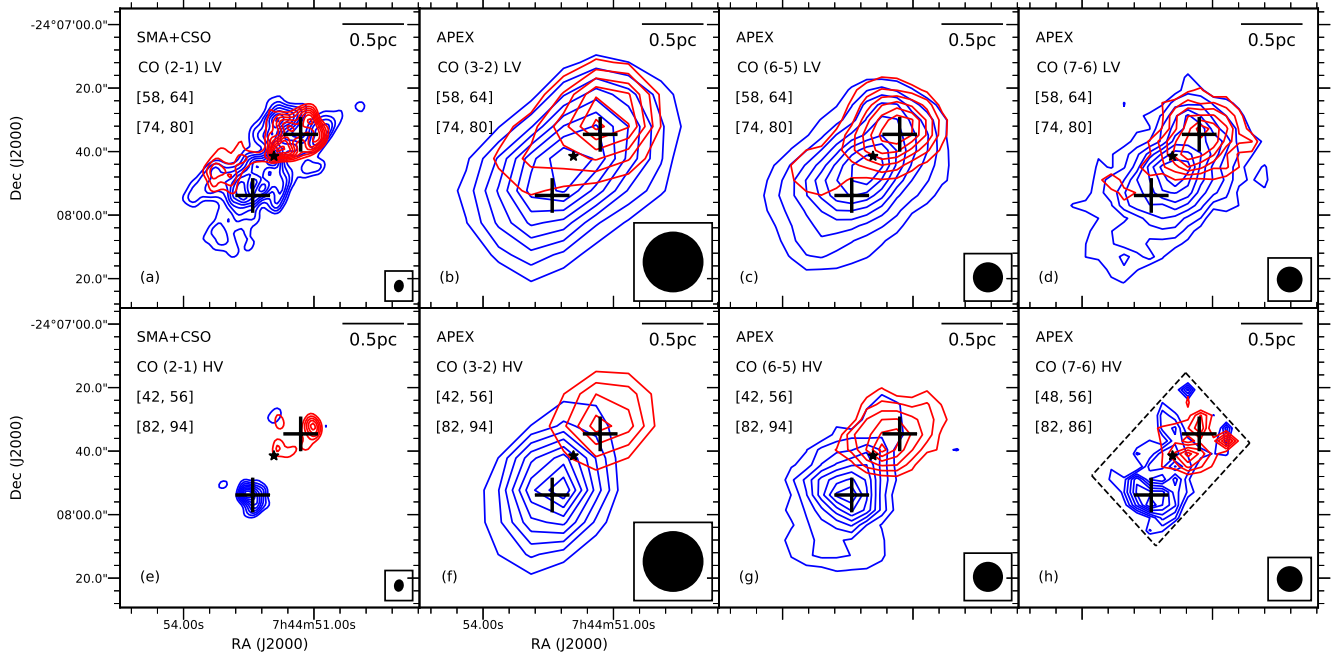
Figure 1. (a)-(d) Low-velocity CO J = (2-1), (3-2), (6-5), (7-6) emissions, integrated from 58 to 64 km s^{-1} for the blueshifted lobe (blue) and from 74 to 80 km s^{-1} for the redshifted lobe (red); (e)-(g) High-velocity CO J = (2-1), (3-2), (6-5), emissions, integrated from 42 to 56 km s^{-1} for the blueshifted lobe (blue) and from 82 to 94 km s^{-1} for the redshifted lobe (red); (h) High-velocity CO J = (7-6) emission, integrated from 48 to 56 km s^{-1} for the blueshifted lobe (blue) and from 82 to 86 km s^{-1} for the redshifted lobe (red). For (a)-(g), the contour levels start from 20% and continue at steps of 10% of the peak emission. For (h), the contour levels start from 30% and continue at steps of 10% of the peak emission. Data outside the dashed region are masked out because of the low signal-to-noise ratio. The black star marks the position of a H$_2$O maser spot which is associated with IRAS 07427-2400 (Sakai et al. 2015). The beam of each observational dataset is shown in the lower right corner of each panel.

transitions. All line ratios in Figure 2 are remarkably constant with velocity. Considering that the ^{13}CO (2-1) emission was only marginally detected in the outflowing gas with high sensitivity observations(Qiu et al. 2009), we assumed the four transitions of ^{12}CO to be optically thin during the analyses. Both the calibration error and the rms noise were taken into account in the belowing analyses.

In a first step, we performed a simple rotation diagram (RD) analysis (Goldsmith & Langer 1999) to estimate the excitation conditions of the outflowing gas in each velocity interval under the assumption of local thermal equilibrium (LTE). The population of each level is given by

$$N_{\rm up} = \frac{N_{\rm CO}}{Z} g_{\rm up} e^{-E_{\rm up}/kT_{\rm kin}}, \qquad (1)$$

where $N_{\rm up}$ is the column density in the upper state, $g_{\rm up}$ the statistical weight of the upper state, $E_{\rm up}$ the upper energy level, k the Boltzmann constant, and Z is the partition function. The rotation diagram for CO at 84 km s^{-1} is shown in Figure 3 as an example. Similar ro-
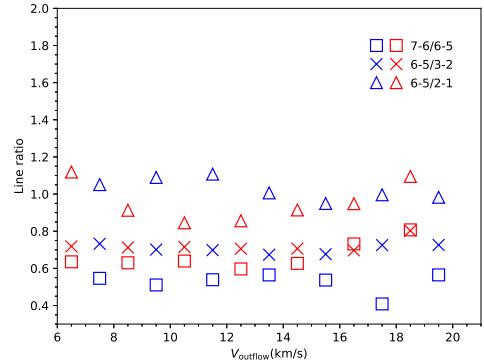

Figure 2. Ratios of main-beam temperatures of different CO lines at different velocities. Blue symbols denote the measurements from the blueshifted lobe, and red symbols the redshifted lobe. The $V_{\rm outflow}$ shown here is related to the cloud velocity $v_{\rm cloud}$ by the relation: $V_{\rm outflow} = \mid v_{\rm outflow} - v_{\rm cloud} \mid$, where $v_{\rm outflow}$ is the outflow velocity with respect to the local standard of rest.
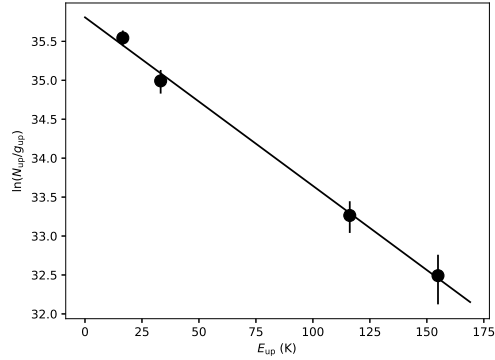
Figure 3. A rotation diagram for CO at 84 km s^{-1}. The fitted line shows the Boltzmann distribution of the rotational populations. The black solid circles show the data with error bars.

tation diagrams were found at other velocities. It should be noted that the different energy levels in each velocity bin could be well reproduced with a single-component excitation condition, indicating that the four transitions probe the same volume of gas.

In a second step, the non-LTE radiative transfer code RADEX (van der Tak et al. 2007) was used to better constrain the gas density (n_{H_2}), the kinetic temperature (T_{kin}) and the CO column density (N_{CO}) of the outflowing gas in each 2 km s^{-1} bin in the Large Velocity Gradient (LVG) approximation. The best fitting results were obtained by minimizing the χ^2_{red} between the observed intensities and the model intensities. With four lines observed and three parameters to constrain, our fitting has one degree of freedom. We didn't correct our observed intensities with beam-filling factors. Thus, the derived physical parameters are the average values over the beam. In Figure 4, the fitting results at 84 km s^{-1} are shown as examples of the χ^2_{red} distribution. Similar χ^2_{red} distribution profiles were found at other velocities. The χ^2_{red} has only one minimum in $[T, N]$ planes. The χ^2_{red} distribution in the $[T, n]$ and $[n, N]$ planes show that the gas is thermalized and no upper limits to the density could be derived, which confirms the LTE assumption used in the rotation diagram analysis. The χ^2_{red} of the best fitting results varies from 0.10 to 1.72 at different velocities. Though the best-fitted χ^2_{red} have different values at different velocities, the χ^2_{red} distributions show similarity in morphology, indicating that the uncertainties of the fitted parameters may have similar level at different velocities. So we derive the uncertainties of each parameter of the LVG analysis from the 1σ confidence region in the N-T-n 3-dimensional space at the velocities where $\chi^2_{red} \sim 1$ as the representative uncertainties of the fitted parameters. The 1σ

confidence ranges of temperatures are about 40 K - 60 K. The lower limits of gas densities (n_{lower}) are around 10^5 cm^{-3}, larger than the critical densities of the four lines. The uncertainties of CO column densities are $\sim$ 10 %. The modeling results predict that the four transitions are optically thin in the outflowing gas, which is consistent with our assumptions. Figure A1 shows the comparison of the observed CO intensities with the LVG modeling results in each velocity bin.

Figure 5 shows the outflowing gas temperature and the CO column density as functions of gas velocity, estimated from the rotation diagram analysis and the LVG analysiss. The N-V diagram shows a clear decreasing trend of CO column density with outflow velocity, while the T-V diagram shows that the gas temperature has no obvious dependence on gas velocity. The best fitted χ^2_{red} at different velocities calculated from the LVG analysis are shown in the N-V diagram.

We then performed the rotation diagram analysis and the LVG analysis again with the line intensities calculated from several different positions and got similar results with previous analysis. Thus, we exclude the systematic bias from the choice of positions for measuring the line intensities.

4. DISCUSSION

Though the morphology and kinematics of molecular outflows have been widely studied, some other physical properties (e.g., the variation of temperature and density with velocity and distance) of molecular outflows are still unclear. High sensitivity CO mid-J observations as complements of existed low-J observations are required to constrain the temperature and density of the molecular outflows as a function of velocity, while these mid-J observations are challenging because of atmospheric limits. There are only several studies on the the $T - V$ relation of molecular outflows. A rising CO 3-2/6-5 ratio is observed towards the outflow associated with low-mass YSO HH 46 IRS 1(van Kempen et al. 2009a). With the density assumed to be constant, the rising ratios at more extreme velocities correspond to lower kinetic temperatures. In the case of the outflow associated with low-mass protostars NGC 1333 IRAS 4A and IRAS 4B, the CO 3-2/6-5 ratios are remarkably constant with velocity (Yıldız et al. 2012). With the assumption of constant density, the constant ratios indicate constant temperatures. In the high-mass case, Su et al. (2012) have imaged the extremely high velocity outflow in CO (2-1) and CO (3-2) associated with the high-mass YSO G5.89-0.39. With the assumption of a canonical CO fractional abundance of 10^{-4}, an increasing trend of temperature with outflow velocity is found
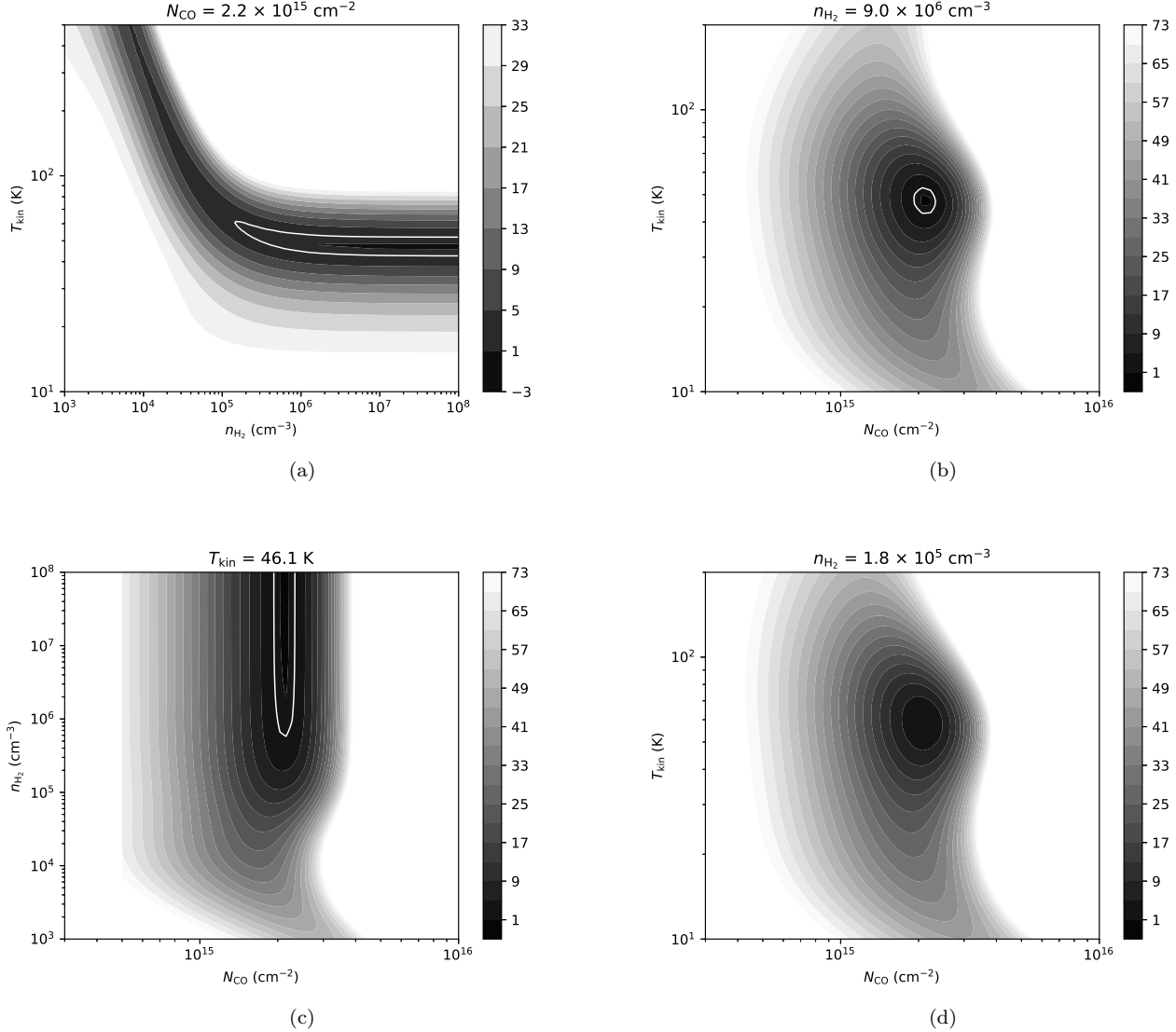
Figure 4. (a)-(c) The $\chi^2_{\rm red}$ distribution at 84 km s^{-1} in the $[T, n]$, $[T, N]$ and $[n, N]$ planes, with all other parameters fixed to the values of the best fitting results at this velocity; (d) The $\chi^2_{\rm red}$ distribution at 84 km s^{-1} in the $[T, N]$ plane, with the density fixed to the lower limit of density in the 1σ confidence region of the fitting result at this velocity. The $\chi^2_{\rm red}$ of the best fitting result is $\sim$1.00 at 84 km s^{-1}. The Solid white contours show the 1σ confidence levels.

by performing a LVG analysis. Using the CO (6-5), (7-6) and (16-15) lines, Leurini et al. (2015) performed a RD analysis towards the G5.89-0.39 outflow and found a decreasing trend of temperature with increasing velocities. This disagreement seen in results of Su et al. (2012) and Leurini et al. (2015) could be due to different angular resolutions (3″.4 compared to 14″.5) and different energy range ($\Delta E_u \sim 17$K compared to $\Delta E_u \sim 600$K). The different $T - V$ relations found in different outflows and in different angular scales reveal the complexity of the molecular outflows. However, with only two or three lines observed, their derived $T - V$ relations must be deduced from fixing other physical parameters, e.g., con-

stant density or constant canonical CO fractional abundance, or from the assumption that the different transitions can be discribed with the same excitation temperature (LTE), while these assumptions might deviate from the real case. To more accurately determine the outflow properties such as the temperature and density, multi-line CO studies with more sophisticated radiative transfer methods (e.g. LVG) are required. So we perform a multi-transition CO study of the G240 outflow, which is representative of a well-defined bipolar wide-angle molecular outflow of in a $> 10^4 L_\odot$ star-forming region (Qiu et al. 2009).
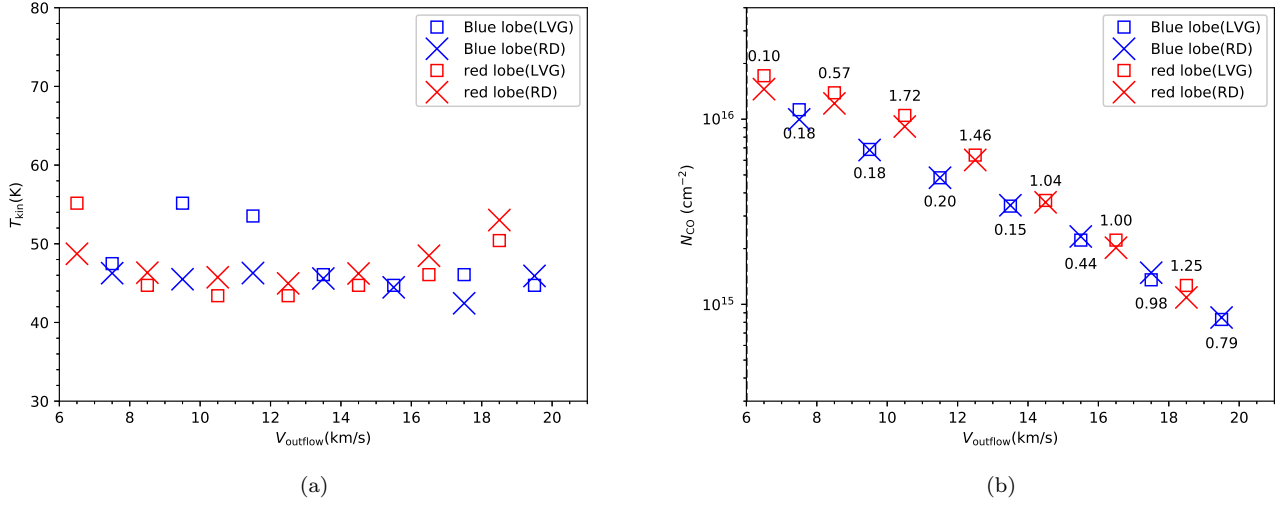
Figure 5. T-V and N-V diagrams of the G240 outflow, estimated from the rotation diagram analysis (blue x marker for blue lobe and red x marker for red lobe) and the LVG analyses (blue open squares for blue lobe and red open squares for red lobe). The best fitted $\chi^2_{\rm red}$ calculated from the LVG analysis are shown in the N-V diagram.

Our analyses reveal that the G240 outflow is isothermal and has a temperature of ~ 50 K, warmer than previously adopted ~ 30 K (Qiu et al. 2009). Thus, the physical parameters (mass, momentum, energy) of the G240 outflow calculated by Qiu et al. (2009) were underestimated by a factor of 1.32. The temperature value of ~ 50 K is consistent with temperatures in excess of 50 K probed by van Kempen et al. (2016) for outflows associated with intermediate-mass protostars, and slightly lower than temperatures of outflows associated with low-mass protostars (van Kempen et al. 2009a; Yıldız et al. 2012). The isothermal state rules out the jet-driven bow shock models, which predicts temperature rising with outflow velocity and distance, and provides evidence for the wind-driven model (Arce et al. 2007). As molecular cooling dominates the cooling of the shocked material in the outflow at temperatures below 10^4 K (Hollenbach 1997) and the cooling rate increases as n^2, molecular cooling is very efficient for the typical density of a wind-driven outflow. Thus, an isothermal state could be reached in a wind-driven outflow. We noticed that there are faint bow-shaped H_2 features near the YSO IRAS 07427-2400, suggesting that the jet-driven outflows may also exist. However, as the beam-averaged T-V relation of the outflowing gas agrees with the wind-driven model and the kinematics and morphology of the molecular outflow can also be qualitatively interpreted by the wide-angle wind-driven model (Qiu et al. 2009), we conclude that even if the jet-driven outflows and the wind-driven outflows were coexisting in the G240 outflow, the wide-angle wind entrainment plays a more im-

portant role in driving the G240 outflow. Mid-J CO observations with higher resolution (e.g. ALMA) are required to study the physical properties of the G240 outflow in detail. It should be noted that, most existing outflow models have parameters typical of outflows driven by low-mass YSOs. It is necessary to compare the observational results with outflow models with physical parameters of outflows from massive YSOs. Statics of outflows associated with high-mass star-forming regions are also essential for us to better understand the driven mechanism of massive outflows and the forming process of high-mass stars.

The LVG analysis reveals that the lower limits of gas densities are $\sim 10^5$ cm^{-3} at the velocities where $\chi^2_{\rm red} \sim 1$. We have found a decreasing trend of the beam-averaged CO column density with gas velocity. As shown in the N-V diagram of Figure 4, for each velocity bin (2 km s^{-1}), the beam-averaged CO column density drops from $\sim 2 \times 10^{16}$ cm^{-2} to $\sim 8 \times 10^{14}$ cm^{-2} within 15 km s^{-1}. In the optically thin case, the beam-averaged CO column density could be related to gas density $n_{\rm H_2}$ through the expression:

$$N_{\rm CO} = n_{\rm H_2} \times \Delta V \times \frac{1}{dv/dr} \times X_{\rm CO} \times f_{\rm b}, \qquad (2)$$

where $f_{\rm b}$ is the beam filling factor, $X_{\rm CO}$ the CO/H_2 abundance ratio, ΔV the velocity interval and dv/dr is the velocity gradient. The CO culumn density is degenerated with the beam filling factor and the abundance ratio. A drop in $N_{\rm CO}$ at more extreme velocities indicates the decrease of one or serveral of these parameters. To explore how the effect of beam dilution influence our

results, we vary the beam filling factors from 0.2 to 1 and then perform the LVG analysis again. We find that modelling with different beam filling factors mainly affect the N-V diagram, with minor change in the T-V diagram and density limits. The derived CO column densities should be considered as lower limits in each velocity bin. This could be resulted from the degeneracies of the beam filling factor with CO column density in the optically thin case.

As shown in Figure 3 of Qiu et al. (2009), the source size are $\sim 20''$ and $\sim 10''$ at the velocities of $\sim \pm 6$ km s^{-1} and $\sim \pm 20$ km s^{-1} with respect to the cloud velocity, corresponding to beam filling factors of ~ 0.5 and ~ 0.2, respectively. Considering the 2.5 times drop in the beam filling factor, the 25 times drop in the beam-averaged CO column density indicates ~ 10 times decrease in the CO column density. Due to the lack of other informations, we cannot assess whether the CO abundance ratio or the velocity gradient has attributed to the drop of CO column density at high velocities. If we assume the CO abundance ratio and the velocity gradient to be constant, the decrease of CO column density could be interpreted by a decrease of gas density with velocity. This decreasing trend is consistent with the wind-driven models which predict that the wind density decreases with velocity and distance from the driving source (Arce et al. 2007).

5. SUMMARY

We have presented the first CO multi-transition (CO 2-1, 3-2, 6-5, 7-6) study towards the molecular outflow of the high-mass star-forming region G240. The morphologies seen in the emission maps of four lines are very similar and the line ratios of the four transitions are remarkably constant with the outflow velocity. With the LVG analysis, we have constrained the temperatures to ~ 50 K and found a decreasing trend of CO column density with gas velocity. We also constrain the H$_2$ density to values higher than $n \sim 10^5$ cm^{-3} and found that the outflowing gas is thermalized. With the RD analysis, we found similar results of the LVG analysis in the temperature and the CO column density. The T-V relation of the G240 outflow agrees well with the wide-angle wind-driven model. Assuming a constant CO abundance ratio and a constant velocity gradient, we detect a decreasing gas density with velocity. A decreasing gas density with velocity is also consistent with the wide-angle wind-driven model.

REFERENCES

Arce, H. G., Shepherd, D., Gueth, F., et al. 2007, Protostars and Planets V, 245

Banerjee, R., & Pudritz, R. E. 2006, ApJ, 641, 949

Beuther, H., Schilke, P., Sridharan, T. K., et al. 2002, A&A, 383, 892

Beuther, H., Schilke, P., Gueth, F., et al. 2002, A&A, 387, 931

Caswell, J. L. 1997, MNRAS, 289, 203

Caswell, J. L. 2003, MNRAS, 341, 551

Frank, A., Ray, T. P., Cabrit, S., et al. 2014, Protostars and Planets VI, 451

Goldsmith, P. F., & Langer, W. D. 1999, ApJ, 517, 209

Hollenbach, D. 1997, Herbig-Haro Flows and the Birth of Stars, 182, 181

Hughes, V. A., & MacLeod, G. C. 1993, AJ, 105, 1495

Kumar, M. S. N., Fernandes, A. J. L., Hunter, T. R., Davis, C. J., & Kurtz, S. 2003, A&A, 412, 175

Lee, C.-F., Mundy, L. G., Reipurth, B., Ostriker, E. C., & Stone, J. M. 2000, ApJ, 542, 925

Lee, C.-F., Stone, J. M., Ostriker, E. C., & Mundy, L. G. 2001, ApJ, 557, 429

Lee, C.-F., Mundy, L. G., Stone, J. M., & Ostriker, E. C. 2002, ApJ, 576, 294

Lefloch, B., Gusdorf, A., Codella, C., et al. 2015, A&A, 581, A4

Leurini, S., Wyrowski, F., Wiesemeyer, H., et al. 2015, A&A, 584, A70

Machida, M. N., Inutsuka, S.-i., & Matsumoto, T. 2008, ApJ, 676, 1088-1108

MacLeod, G. C., Scalise, E., Jr., Saedt, S., Galt, J. A., & Gaylard, M. J. 1998, AJ, 116, 1897

Masson, C. R., & Chernin, L. M. 1993, ApJ, 414, 230

Maud, L. T., Moore, T. J. T., Lumsden, S. L., et al. 2015, MNRAS, 453, 645

Migenes, V., Horiuchi, S., Slysh, V. I., et al. 1999, ApJS, 123, 487

Pudritz, R. E., Rogers, C. S., & Ouyed, R. 2006, MNRAS, 365, 1131

Pudritz, R. E., Ouyed, R., Fendt, C., & Brandenburg, A. 2007, Protostars and Planets V, 277

Qiu, K., Zhang, Q., Wu, J., & Chen, H.-R. 2009, ApJ, 696, 66

Qiu, K., Zhang, Q., Menten, K. M., et al. 2014, ApJL, 794, L18

Raga, A., & Cabrit, S. 1993, A&A, 278, 267

Ren, J. Z., Liu, T., Wu, Y., & Li, L. 2011, MNRAS, 415, L49

Sakai, N., Nakanishi, H., Matsuo, M., et al. 2015, PASJ, 67, 69

Shang, H., Allen, A., Li, Z.-Y., et al. 2006, ApJ, 649, 845

Shepherd, D. S., Watson, A. M., Sargent, A. I., & Churchwell, E. 1998, ApJ, 507, 861

Shu, F. H., Ruden, S. P., Lada, C. J., & Lizano, S. 1991, ApJL, 370, L31

Shu, F. H., Najita, J. R., Shang, H., & Li, Z.-Y. 2000, Protostars and Planets IV, 789

Su, Y.-N., Liu, S.-Y., Chen, H.-R., & Tang, Y.-W. 2012, ApJL, 744, L26

Trinidad, M. A. 2011, AJ, 142, 147

van der Tak, F. F. S., Black, J. H., Schöier, F. L., Jansen, D. J., & van Dishoeck, E. F. 2007, A&A, 468, 627

van Kempen, T. A., van Dishoeck, E. F., Güsten, R., et al. 2009, A&A, 501, 633

van Kempen, T. A., van Dishoeck, E. F., Güsten, R., et al. 2009, A&A, 507, 1425

van Kempen, T. A., Hogerheijde, M. R., van Dishoeck, E. F., et al. 2016, A&A, 587, A17

Wu, Y., Wei, Y., Zhao, M., et al. 2004, A&A, 426, 503

Wu, Y., Zhang, Q., Chen, H., et al. 2005, AJ, 129, 330

Yıldız, U. A., Kristensen, L. E., van Dishoeck, E. F., et al. 2012, A&A, 542, A86

Zhang, Q., Hunter, T. R., Brand, J., et al. 2001, ApJL, 552, L167
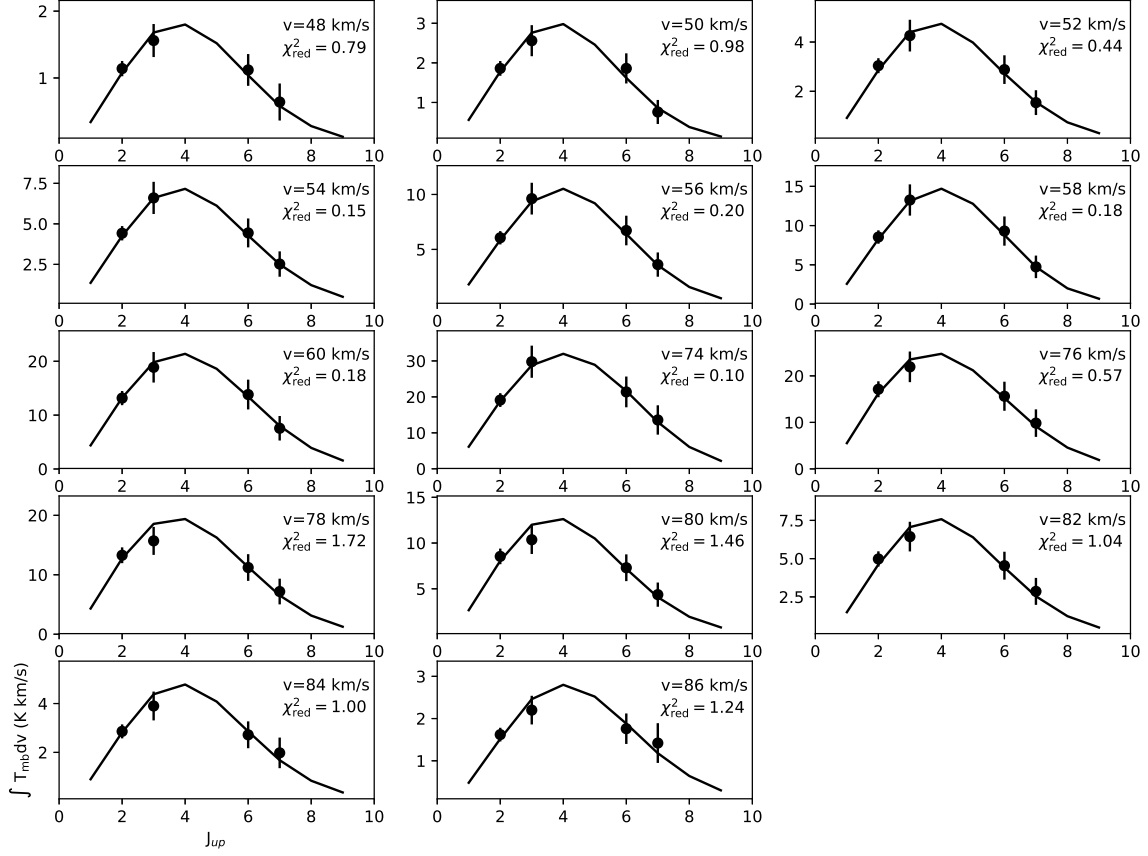
APPENDIX

A. LINE INTENSITY DISTRIBUTIONS

Figure A1. Observed line fluxes compared with the LVG model fitting results in each 2 km/s bin. The black solid circles show the observed data with error bars. The black solid lines refer to the best fits. The outflow velocities and the χ^2_{red} of the best fitting results are shown in each panel.